

Polarization Performance Simulation for the GeoXO Atmospheric Composition Instrument: NO₂ Retrieval Impacts

Aaron Pearlman^{1,3}, Monica Cook^{1,3}, Boryana Efremova^{1,3}, Francis Padula^{1,3}, Lok Lamsal^{2,3}, Joel McCorkel³, and Joanna Joiner³

¹GeoThinkTank LLC, Miami, FL, USA

²University of Maryland Baltimore County (UMBC), Baltimore, MD, USA

³NASA Goddard Space Flight Center, Greenbelt, MD, USA

Correspondence: Aaron Pearlman (aaron@geothinktank.com)

Abstract. NOAA's Geostationary Extended Observations (GeoXO) constellation will continue and expand on the capabilities of the current generation of geostationary satellite systems to support US weather, ocean, atmosphere, and climate operations. It is planned to consist of a dedicated atmospheric composition instrument (ACX) to support air quality forecasting and monitoring by providing similar capabilities to missions such as TEMPO (Tropospheric Emission: Monitoring Pollution), currently planned to launch in 2023, and Ozone Monitoring Instrument (OMI), TROPOMI (TROPOspheric Monitoring Instrument), and GEMS (Geostationary Environment Monitoring Spectrometer) currently in operation. As the early phases of ACX development are progressing, design trade-offs are being considered to understand the relationship between instrument design choices and trace gas retrieval impacts. Some of these choices will affect the instrument polarization sensitivity (PS), which can have radiometric impacts on environmental satellite observations. We conducted a study to investigate how such radiometric impacts can affect NO₂ retrievals by exploring their sensitivities to time of day, location, and scene type with an ACX instrument model that incorporates PS. The study addresses the basic steps of operational NO₂ retrievals: the spectral fitting step and the conversion of slant column to vertical column via the air mass factor (AMF). The spectral fitting step was performed by generating at-sensor radiance from a clear sky scene with a known NO₂ amount, the application of an instrument model including both instrument PS and noise, and a physical retrieval. The spectral fitting step was found to mitigate the impacts of instrument PS. The AMF-related step was considered for clear sky and partially cloudy scenes, where instrument PS can lead to errors in interpreting the cloud content, propagating to AMF errors and finally to NO₂ retrieval errors. For this step, the NO₂ retrieval impacts were small but non-negligible for high NO₂ amounts; we estimated that a typical high NO₂ amount can cause maximum of 0.25×10^{15} molecules/cm² for a PS of 5%. These simulation capabilities were designed to aid in the development of a GeoXO atmospheric composition instrument that will improve our ability to monitor and understand the Earth's atmosphere.

Copyright statement. TEXT

1 Introduction

NOAA's Geostationary Extended Observations (GeoXO) constellation will continue and expand on the capabilities of the current generation of geostationary satellite systems to support US weather, ocean, atmosphere, and climate operations. It is planned to consist of a dedicated atmospheric composition instrument to support air quality monitoring and forecasting. The mission will build on knowledge obtained from low earth orbit (LEO) and geostationary (GEO) satellite air quality monitoring instruments such as TROPOMI (TROPOspheric Monitoring Instrument) (Veefkind et al. (2012)), Ozone Monitoring Instrument (OMI) (Leveld et al. (2006, 2018)), Geostationary Environment Monitoring Spectrometer (GEMS) Hollingsworth et al. (2008), and SENTINEL 4 (Kolm et al. (2017)). Retrievals of trace gases like NO₂ derived from satellite platform observations have been used to relate top-down emissions estimates, air quality monitoring and forecasting, pollution events, trends, and health studies (Bovensmann et al. (2011); Leveld et al. (2018); Burrows et al. (1999); Bovensmann et al. (1999); Leveld et al. (2006); Munro et al. (2016); Bak et al. (2017); Veefkind et al. (2012); Cooper et al. (2022)). The World Health Organization has designated NO₂ as a pollutant, since it has detrimental effects on human health (WHO (2021); Huangfu and Atkinson (2020)). It also impacts climate by contributing to the formation of aerosols in the upper troposphere that reflect incoming solar radiation, and, thus, cool the planet (Shindell et al. (2009)). Over non-polluted regions, the stratospheric NO₂ participates in photochemical reactions that can affect the ozone layer (van Geffen et al. (2020)).

In the near future, these phenomena will be monitored from geostationary (GEO) orbit over the greater North America as part of the TEMPO (Troposphere Emission: Monitoring Pollution) mission (Zoogman et al. (2017)), at an increased temporal frequency than available from its LEO counterparts. Like other atmospheric composition monitoring instruments, TEMPO is and ACX will be a hyperspectral imager with fine spectral sampling and resolution from the ultraviolet to the near-infrared allowing trace gas absorption features to be discriminated using the well-known differential optical absorption spectroscopy (DOAS) technique. For total vertical NO₂ amount retrievals, the DOAS technique is applied around the 420 to 455 nm range (Bucsela et al. (2006); Lamsal et al. (2021); Marchenko et al. (2015); Boersma et al. (2007); Richter and Burrows (2002); Valks et al. (2011); Martin (2002)).

ACX is in its early stages of development with its initial performance requirements being developed with respect to parameters like sampling and resolution to enable this DOAS approach. Other parameters such as pixel size, noise, and polarization sensitivity (PS) are also being defined. These requirements may be updated as the instrument design choices are better understood. This study focuses on the requirements for instrument PS, which is known to impact the at-sensor radiance for polarization-sensitive satellites sensors in geostationary (GEO) (Pearlman et al. (2015)) and low Earth orbit (LEO), though more extensively analyzed for LEO satellites (Meister and Franz (2011); Wu et al. (2017); Goldin et al. (2019)).

GEO orbit presents unique challenges due to the highly variable solar angles throughout the day. This results in a variation in the degree of linear polarization of the at-sensor radiance throughout the day due to Rayleigh scattering in the Earth's atmosphere; for instance, light scattered in the normal direction to the incident light generates highly polarized radiation but not in the forward or backward direction. Limiting the PS of the satellite sensor limits the radiometric uncertainty. These impacts

55 can be derived by employing radiative transfer simulations to predict the at-sensor polarization state or Stokes parameters (S) and applying the instrument polarization impacts via its Mueller matrix (M).

$$\mathbf{S} = [\mathbf{S}_0 \mathbf{S}_1 \mathbf{S}_2 \mathbf{S}_3]^t \quad (1)$$
$$\mathbf{S}' = \mathbf{M} \mathbf{S}$$

The Stokes formulation expresses the polarization state consisting of its un-polarized (or randomly polarized) component, S_0 ; two terms describe its linear polarization state: the excess in horizontal linear polarization relative to the vertical direction, 60 S_1 , and excess in linear polarization at 45° relative to 135° , S_2 ; one term describing its circular through its excess of right circular relative to left circular polarization, S_3 . The Mueller matrix is a 4×4 matrix used to apply the optical effects of an element to generate an output Stokes vector. We model ACX as a Mueller matrix with a transmission of one and non-zero linear polarization extinction elements (m_{01}, m_{02}, m_{10} , and m_{20}). Since the system only detects total energy or radiance, not polarization state, only the first row is relevant. So the output term corresponding to the detected normalized Stokes parameter 65 is:

$$S'_{ACX} = 1 + m_{01}S_1 + m_{02}S_2 \quad (2)$$

This detected radiance can differ from the true at-sensor radiance if ACX has linear PS, defined as $\sqrt{(m_{01}^2 + m_{02}^2)}$, which can propagate to higher level satellite products. For instance, the retrieval of surface reflectance can suffer large uncertainties, especially when the signal from the surface is small compared to the atmospheric component. In this work, we discuss our study 70 of NO_2 retrievals, and investigate the parts of the process that may be affected. To our knowledge, NO_2 retrievals dependence on instrument PS have not yet been fully documented. We describe an initial study to show the ways that these retrievals can be impacted and make initial estimates of those impacts associated with the current PS requirements, $<5\%$ PS for wavelengths <500 nm.

Our NO_2 retrieval simulation approach discussed here follows a simplified version of the DOAS technique used for operational NO_2 retrievals and consists of two basic steps: One involves the DOAS spectral fitting step for the at-sensor radiance. 75 This fit is normally used to retrieve the NO_2 slant column amount —the total number of molecules along the atmospheric photon path to the satellite sensor. The second step converts this slant column amount to the vertical column amount through the air mass factor (AMF), which depends on the geometrical path as well as the differences in scattering and absorption within the atmosphere between the slant and vertical paths. Our first approach for analyzing polarization effects deals with the DOAS 80 spectral fitting step with clear sky scenes by simulating at-sensor Stokes parameters and applying an instrument model that includes a range of PS values in several orientations (defined by m_{01} and m_{02}), as well as the instrument noise and spectral properties consistent with our current knowledge of ACX. The fits of these spectra are used to retrieve NO_2 vertical column amount directly, not slant column, in our case; since these are simulations with the vertical profiles used as inputs, we do not need to use the AMF for converting slant column to vertical column amount. The second approach deals exclusively with 85 the AMF derivation step. For this analysis, the AMF, required for operational retrievals, is affected by instrument PS when

considering the potential for partially cloudy scenes. Retrievals in such situations are commonly performed for atmospheric monitoring instruments, since their large instantaneous fields of view make completely clear scenes rare. We will discuss the formalism in detail for both approaches in the methods section. With these two approaches, referred to as the method for "clear scenes" and "partially cloudy scenes", we demonstrate the capability to investigate PS requirements.

90 2 Methods

As mentioned, the approach for clear scenes exploits the spectral features in the radiance spectra to retrieve the total vertical amount of NO₂, and the approach for cloudy scenes relies on the AMF calculation.

2.1 Clear scenes

The overall method for clear scenes is illustrated in Fig. 1. In this process, simulated radiance spectra are propagated through an instrument model and the total vertical column NO₂ is retrieved using a look-up table (LUT) approach with the aid of a constrained energy minimization algorithm (CEM) (Farrand (1997)). Further details are discussed below.

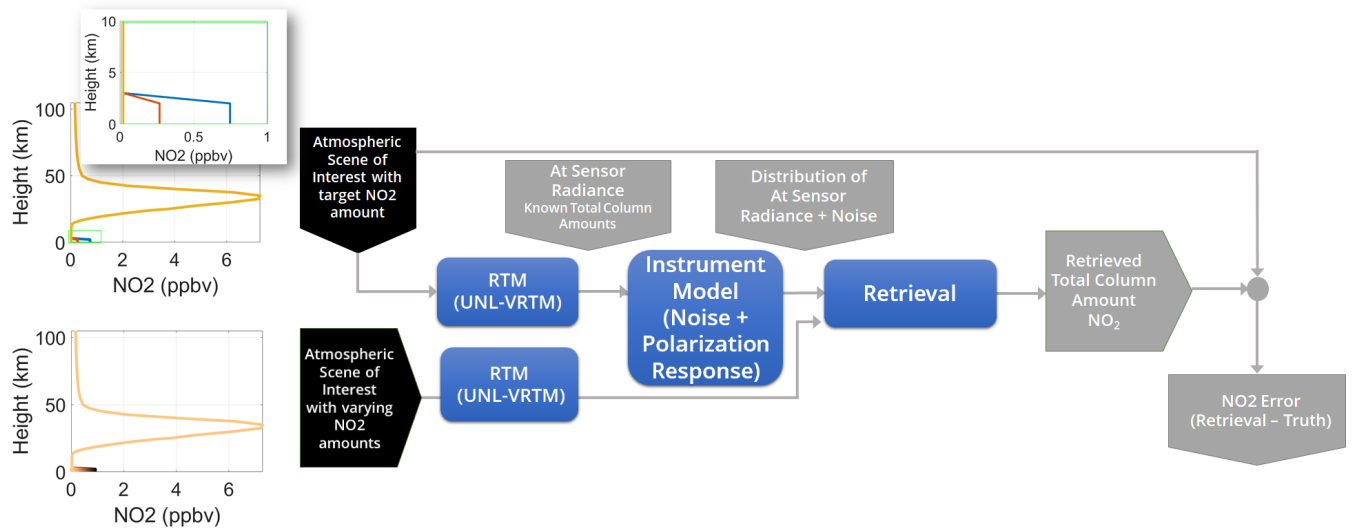


Figure 1. Simulation method for retrieving NO₂ in clear scenes: The scenes of interest consist of selected custom NO₂ profiles to represent low, medium, and high NO₂ cases shown at the upper left (including a zoomed-in view) corresponding to total vertical NO₂ amounts of 4.60, 5.93, and 8.44×10^{15} molecules/cm², respectively. The lower left profiles contain all profiles used in the retrieval process. The profiles are used in the radiative transfer model (RTM) called the Unified Linearized Vector Radiative Transfer Model (UNL-VRMT) to generate at-sensor radiance.

2.1.1 Radiative Transfer Modeling

The at-sensor radiances from clear scenes are simulated using a vector radiative transfer code, the Unified Linearized Vector Radiative Transfer Model, UNL-VRTM, which integrates the linearized vector radiative transfer (VLIDORT) into a broader framework (Xu and Wang (2019)). The code can generate Stokes vectors from any scene defined by its view and solar geometry, surface reflectance, wavelength range, and atmospheric composition. Note that rotational Raman scattering is not included in the model. The ACX was assumed to be at 105° West longitude viewing several locations across the continental US (CONUS). The time of day was chosen to generate solar zenith angles of 60 to 70° , where PS is expected to be highest but still within the range where NO_2 retrievals are typically performed. The US Standard Model default profiles were used for 21 trace gases for all scenes (excluding NO_2). The default NO_2 profiles were modified by injecting a known amount uniformly into the troposphere below 2 km (Fig. 1). Three basic surface spectra generated from spectral libraries were used. The water spectrum used is associated with an open ocean case (Kokaly et al. (2017)); the vegetation is a combination of trees (30 %), grass (30 %), shrubs(30 %), non-photosynthetic material (5 %), and soil (5 %), and the urban case is a combination of roof (50 %), concrete (20 %), road (20 %), and vegetation (10 %) (Meerdink et al. (2019); Baldridge et al. (2009)) as depicted in Fig. 2. Their associated background aerosol content was included in the boundary layer up to 2 km with a uniform vertical distribution. The rural and urban scenes use a bi-modal aerosol distribution as shown in Table 1, where the loading and size distribution values for each mode are given for these scenes. The aerosol parameters including the complex indices of refraction per wavelength were taken from Shettle et al. (1979) with loading values from the climatology reported in Yan et al. (2021).

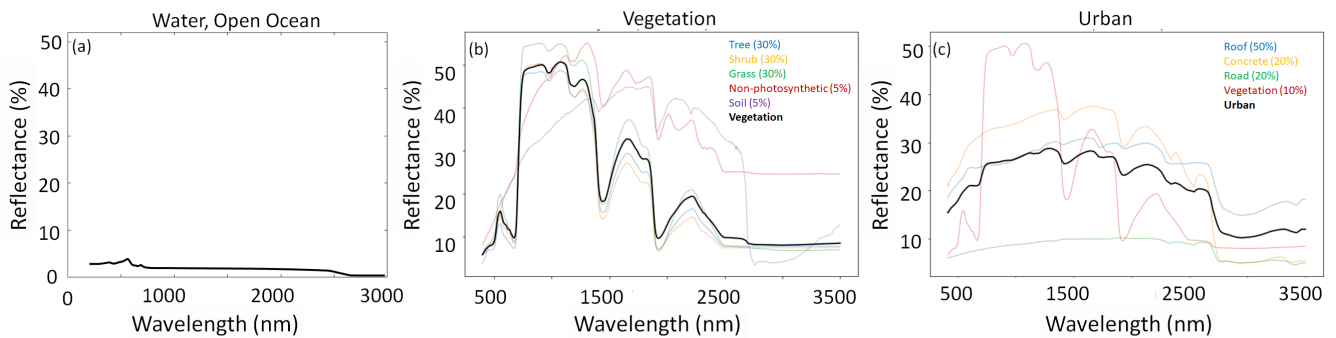


Figure 2. Basic surfaces reflectance spectra used in radiative transfer simulations.

We ran radiative transfer simulations for several US locations, with the three scene types, with varying amounts of tropospheric NO_2 . This produced a look up table (LUT) of scene type, NO_2 vertical amount, and at-sensor radiance spectra. This LUT was used in the retrieval discussed below.

Table 1. UNL-VRTM Parameters

Scene Type	Reflectance Spectrum		Aerosol		
			Index of refraction	Loading (AOD)	Size distribution
					radius [μm]
Water	Open ocean	Sea Salt	1.52	0.08	0.3
Rural	Trees, shrubs, grass, non-photosynthetic, soil	Water soluble, dust	1.52	0.13, 0.42	0.03, 0.5
Urban	Roof, concrete, road, vegetation	Water soluble, soot	1.52	0.03, 0.5	0.03, 0.5

2.1.2 Instrument model and NO_2 retrievals

The reference radiance spectra corresponding to the NO_2 reference amounts over water, rural and urban scenes were modified by applying the instrument model (for several US locations). The simulated radiance was modified by the instrument response model that sampled the radiance at 0.2 nm wavelength steps with a resolution of 0.6 nm and the PS response model. The noise was also applied as defined by the ACX signal-to-noise (SNR) specification. Our instrument parameters from TEMPO were modified by assuming a sampling strategy or integration time modification that brought the noise in line with that specified by ACX. Table 2 shows the parameters included in this model.

Table 2. ACX instrument response model parameters

Parameter	Description
$L(\lambda)$	Spectral radiance at instrument resolution
A_{det}	Detector area
$\Omega = \pi/4(f\#)^2$	Solid angle of acceptance
Δt	Integration time
λ	Wavelength
$\Delta\lambda$	Spectral interval per pixel
$\tau(\lambda)$	Optical system transmittance combined with grating efficiency
$\eta(\lambda)$	Detector quantum efficiency
N	Bit depth
n_{read}	Read noise
I_{dark}	Dark current

The noise was applied by generating 1000 spectra with different amounts of noise following a Gaussian distribution that are added to the at-sensor radiance (after being modified by the polarization response). All spectra were normalized by subtracting

a second order polynomial fit to remove the sensitivity to absolute radiance as is done in the DOAS retrieval technique. The NO₂ vertical amount was retrieved using the look-up-table and the CEM algorithm:

$$\text{CEM} = \frac{(t - m)^T S^{-1} (x - m)}{(t - m)^T S^{-1} (t - m)}, \quad (3)$$

where S^{-1} and m are the inverse covariance matrix and mean over the noise spectra, respectively. The CEM was calculated for

130 all all (target) spectra in the LUT, t , with the noise spectra, S^{-1} and m . The spectrum, x that generated a CEM value closest to one was chosen, and its associated NO₂ vertical amount was retrieved.

2.2 Partially cloudy scenes

The process for "partially cloudy scenes" involves an AMF derivation process that includes the consideration of subpixel-scale clouds. The typical instantaneous field of view for an atmospheric composition instruments means that most scenes contain

135 some clouds. Operational trace gas retrievals are routinely done in partially cloudy scenes, so we derive PS impacts for such scenes primarily through their impact on the AMF.

2.2.1 Theoretical background

This approach assumes a simple cloudy scene model where each scene is assumed to be a combination of a fully cloud covered subpixel and a clear sky subpixel weighted with an effective cloud fraction, f , consistent with previous approaches (Stammes

140 et al. (2008)):

$$L_{obs} = L_{clr}(1 - f) + L_{cld}f, \quad (4)$$

where L_{obs} is the observed radiance, L_{clr} is the calculated radiance in a clear sky, and L_{cld} is the cloudy radiance. To produce

observed amounts of Rayleigh scattering and absorption, it was found that for this equation to work across most conditions, we model L_{clr} as a Lambertian surface (opaque) with surface reflectivity 0.80 at the effective cloud pressure, assumed here to

145 be equivalent to a cloud 2 km. This simple model has been demonstrated to represent the complex radiative transfer in clouds accurately (Stammes et al. (2008); Joiner (2004); Vasilkov et al. (2008)). So, we typically derive f at a wavelength with little absorption and use a surface climatology for L_{clr} . Then, we simply invert the above equation to give:

$$f = \frac{L_{obs} - L_{clr}}{L_{cld} - L_{clr}}. \quad (5)$$

For the trace gas retrievals, another quantity defines the fraction of scene radiance from the cloud versus the clear parts of the

150 scene called the cloud radiance fraction f_r , which has wavelength dependence:

$$f_r = f \frac{L_{cld}}{L_{obs}}. \quad (6)$$

A cloudy air mass factor (AMF) is computed along with the clear sky AMF. The total AMF is then computed with the clear and cloudy AMFs weighted by the cloud radiance fraction

$$\text{AMF}_{tot} = \text{AMF}_{clr}(1 - f_r) + \text{AMF}_{cld}f_r. \quad (7)$$

155 To compute the error in the NO₂ vertical column due to an error in f , we started with the calculation of the error in f due to an error from PS:

$$\frac{df}{d\epsilon_{PS}} = \frac{dL_{obs}}{d\epsilon_{PS}} \frac{1}{(L_{cld} - L_{clr})}, \quad (8)$$

and this would then propagate into the error in NO₂ vertical column density ($NO_{2,VCD}$) through Equations 6,7 above along with:

$$160 \quad NO_{2,VCD} = \frac{NO_{2,SCD}}{\text{AMF}_{tot}}. \quad (9)$$

This process is shown graphically in Fig 3, where a clear and cloudy version of a scene are simulated. The clear version is propagated through the instrument polarization response model, and, using the radiance generated from the cloudy scene, the impacts are propagated through the cloud fraction, cloud radiance fraction, AMF, and finally the NO₂ amount. The AMF was computed using a pre-calculated LUT with input parameters of altitude, z , solar zenith angle, view zenith angle, relative azimuth angle, surface reflectance, and surface altitude. The output AMF was calculated by linearly interpolating over all variables for each altitude and summing over all layers to the top of atmosphere (TOA), where each layer dz has a vertical column amount V_{NO_2} :

$$165 \quad \text{AMF}_{total} = \frac{\int_0^{TOA} \alpha \cdot \text{AMF} \cdot V_{NO_2} dz}{\int_0^{TOA} V_{NO_2} dz}, \quad (10)$$

where the integration assumes an exponential dependence within each layer (Kuhlmann et al. (2015), Berk et al. (2016)). The 170 temperature correction term, α , was neglected by setting it to one. The NO₂ error derived through the conversion of slant to vertical amount is then computed. This error can be considered as the change the PS effect on radiance, which, in turn, leads to an error in the interpretation of the amount of clouds in the scene. This leads to an impact on the NO₂ retrieval over the total vertical column. Note that this changes negligibly as a function of wavelength, so we perform this analysis at one wavelength (425.8 nm) in this study. By differentiating Equation 9, the NO₂ error in the total vertical column amount ($\partial(NO_{2,total})$) is 175 then calculated in terms of the total vertical NO₂ amount ($V_{NO_2,total}$), the AMF, and the AMF error (∂AMF_{tot}) as:

$$175 \quad \partial(NO_{2,total}) = \frac{-V_{NO_2,total}}{\text{AMF}_{total}} \cdot \partial(\text{AMF}_{total}). \quad (11)$$

2.2.2 Radiative transfer modeling

We conducted the radiative transfer simulations over the entire CONUS region using two approaches: assume water, rural, urban scene covers CONUS at one degree latitude/longitude increments for each surface and a given reference NO₂ profile (used in the clear scene method) with times chosen to give constant solar zenith angles; or use NO₂ profiles from the Goddard Earth Observing System Model, Version 5 (GEOS-5) (Molod et al. (2012)) on a particular time and day with a fixed scene type over the CONUS grid. The former method gives a contrived version that is useful for bounding the impacts of instrument PS and isolating impacts of different variables, for instance, NO₂ amount or solar zenith angle. The latter method represents cases with more realistic nominal parameters. Note that we also used the cloud fraction from the GEOS-5 model for deriving the simulated radiance prior to applying the polarization response model. This deviates from the illustration in Fig. 1 (top left), where instead of a clear scene, a mixture of cloudy and clear scene according to the GEOS-5 cloud fraction value is used. A single day was chosen to demonstrate this approach, July 15, 2007 on two selected times 16 UTC and 20 UTC, so that the impacts of extreme solar zenith angles (corresponding to degree of linear polarization) could be seen for both the eastern and western US regions.

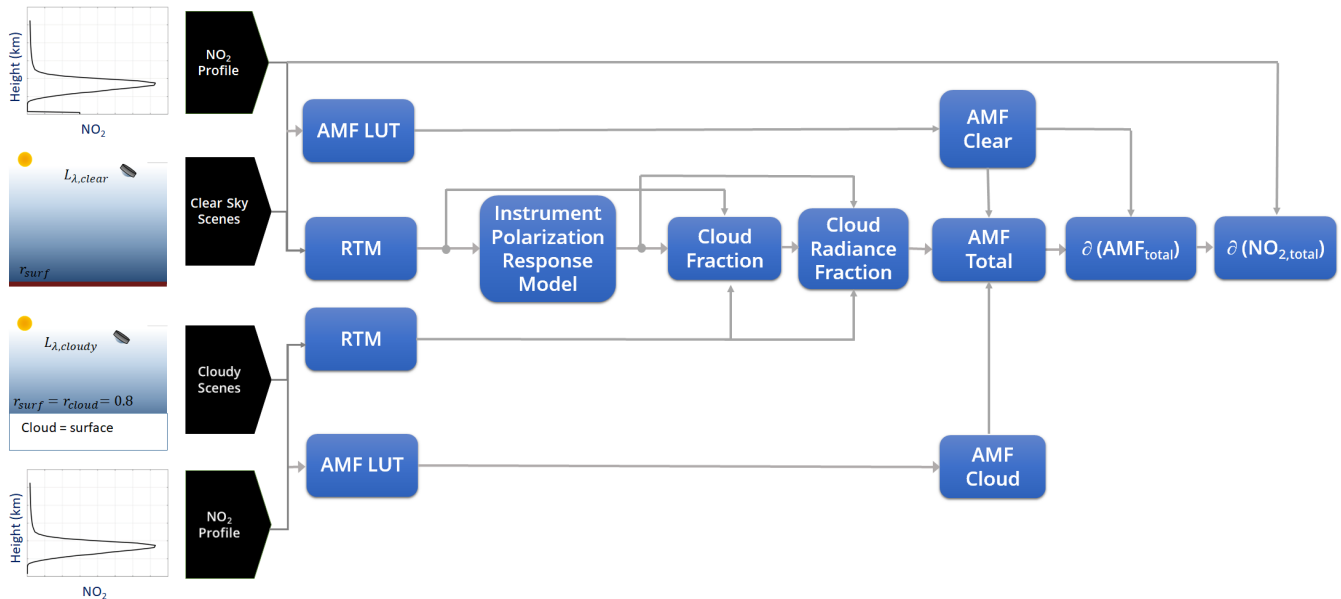


Figure 3. Simulation method for deriving NO₂ errors by interpreting a clear scene as a partially cloudy scene due to instrument PS: Through radiative transfer modeling (RTM) and air mass factor (AMF) calculations via a look-up table (LUT) of clear and cloudy scenes, and applying the instrument polarization response model to a clear scene, the NO₂ error is determined by propagating through the variables shown to errors in AMF ($\delta(AMF_{total})$) and total vertical NO₂ amount ($\delta(NO_{2, total})$)

3.1 Clear scenes

As part of the method for clear scenes, the ACX instrument model was applied to the at-sensor radiance including sampling with a Gaussian slit function at the interval and resolution of 0.2 and 0.6 nm, respectively and its noise as depicted in Fig. 4. The differences between the normalized solar irradiance (multiplied by a factor of 5 for visibility) and radiance spectra shows the atmospheric contribution and the effects of this resampling. The 1000 radiance spectra shown cannot be discerned clearly given the high SNR (explicitly shown by the blue line). The noise was applied after modifying with the PS response. The PS model parameters applied via Equation 2 using $m_{01} = \pm PS$ and $m_{02} = 0$, so that the PS was applied in the vertical or horizontal orientation. These orientations were chosen for most simulations for simplicity but other orientations will be discussed in the cloudy scene analysis section.

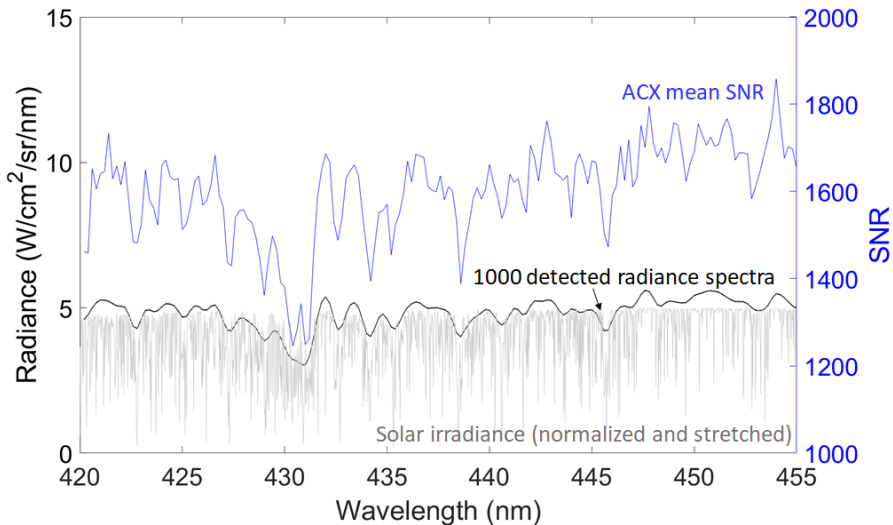


Figure 4. Example of at-sensor radiance spectra simulated with an applied instrument model including resampling effects and added noise set by ACX instrument parameters. 1000 spectra are plotted (black lines), which appears as a slightly thicker line than the mean SNR (blue line and axis). The normalized solar irradiance multiplied by a factor of 5 is shown for comparison to the resampled spectra.

The retrieval process effectively matches the spectral shape of the simulated detected spectra —affected by spectral sampling, noise, and PS —to the most similar spectra in the LUT that contains a large range of tropospheric NO₂ amounts for the three surfaces. Figure 5(a) shows an example of a the adjusted sample spectrum with the the spectra in the LUT. Note that all spectra were adjusted using quadratic fits in the spectral fitting process. The CEM algorithm finds the spectrum from the spectra that is most similar. Figure 5(b) shows a summary of the NO₂ retrieval errors, average biases and standard deviations as a function of PS for several scene types. The errors are driven by the noise and are similar for all scene types. The flat dependence indicates that the PS does not affect the retrieval error in the DOAS spectral fitting retrieval step. The reason is that the PS is a smooth

function of wavelength, and the radiometric error introduced are compensated through the spectral fitting process. These results were similar for all locations (not shown). We note that other retrieval techniques that do not use a spectral fitting approach may exhibit larger PS impacts.

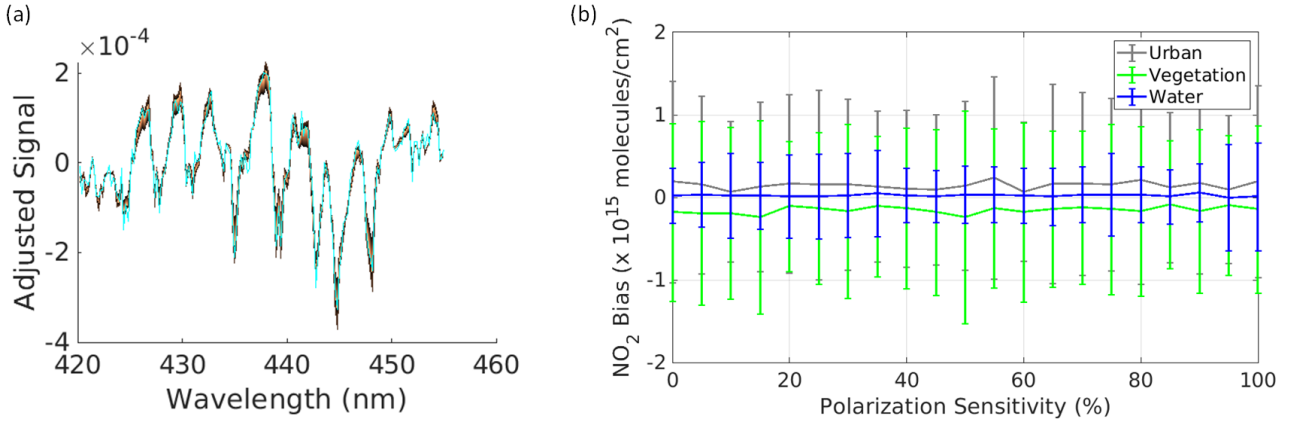


Figure 5. Clear-sky scene retrieval results: (a) An example of an adjusted ACX simulated spectrum (cyan) with all spectra from the look-up-table (LUT) with varying amounts of tropospheric NO_2 (b) The average error (or bias) and standard deviation for 1000 total vertical NO_2 retrievals of the "high" amount (8.44×10^{15} molecules/cm 2) for the three scene types (water, vegetation, and urban) at Norman, Oklahoma, assuming a vertical PS orientation.

210 3.2 Partially cloudy scenes

In contrast to the previous results, the AMF-related processing step showed more significant polarization impacts, where an error is induced when a clear scene scene is interpreted as a partially cloudy scene due to the instrument response model that includes PS (but not noise). Figure 6 shows the results as they are propagated through each step in the process (Fig. 3) for an example with an extremely high total vertical NO_2 amount, 20×10^{15} molecules/cm 2 , over all of CONUS. The 215 simulation ran using 70° solar zenith angle and water scene for all pixels and an instrument PS of 5%, $m_{01} = -0.05$, vertical orientation and $m_{02} = 0.05$, 45° orientation. The Stokes parameter, S_1 is relevant for vertical (or horizontal) polarization and S_2 is relevant for 45° (or 135°) polarization. The correlation between the relevant Stokes parameters, cloud fraction, and NO_2 error are particularly apparent. This example shows that the PS orientation can generate vastly different spatial dependence in NO_2 retrieval errors. The maximum NO_2 error of 1.4×10^{15} molecules/cm 2 is above the specified TEMPO NO_2 precision 220 Zoogman et al. (2017). Note that this is likely an upper bound, since NO_2 amounts like these are mostly found in industrialized areas in other regions of the world.

The remaining cases are more realistic cases for CONUS: Figure 7 shows a lower NO_2 amounts of 8.4×10^{15} molecules/cm 2 corresponding to the "high" NO_2 case shown in Fig. 1. The results are shown for the three different scene types applied across all of CONUS. The other parameters are the same as the previous case. The NO_2 error increases as the surface reflectance

225 decreases. All cases show the same spatial pattern over CONUS as in the previous case. The maximum NO₂ error is 0.25 $\times 10^{15}$ molecules/cm².

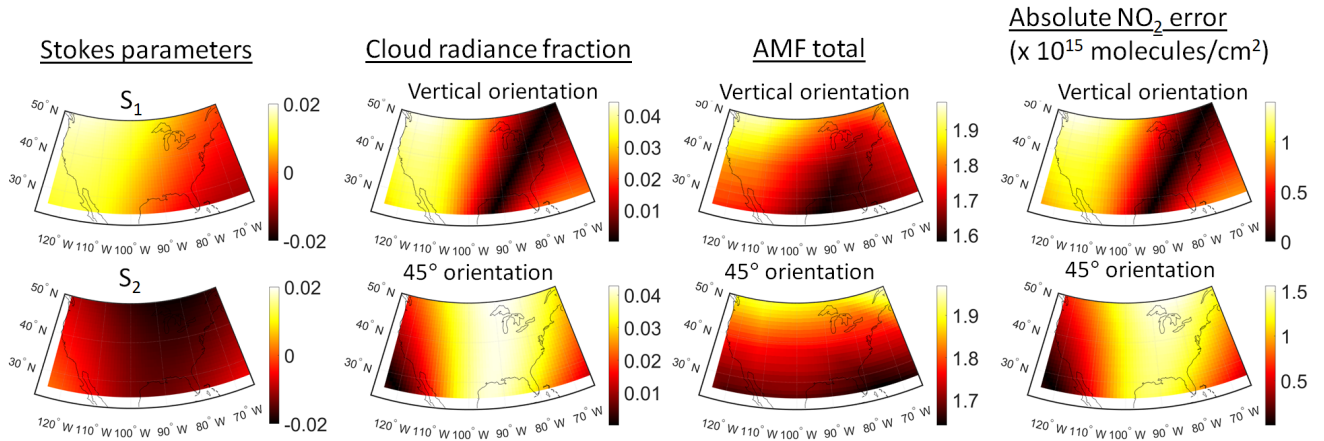


Figure 6. Derived parameters for NO₂ amount of 20×10^{15} molecules/cm², water scenes, and 5% PS in a vertical and 45° orientation

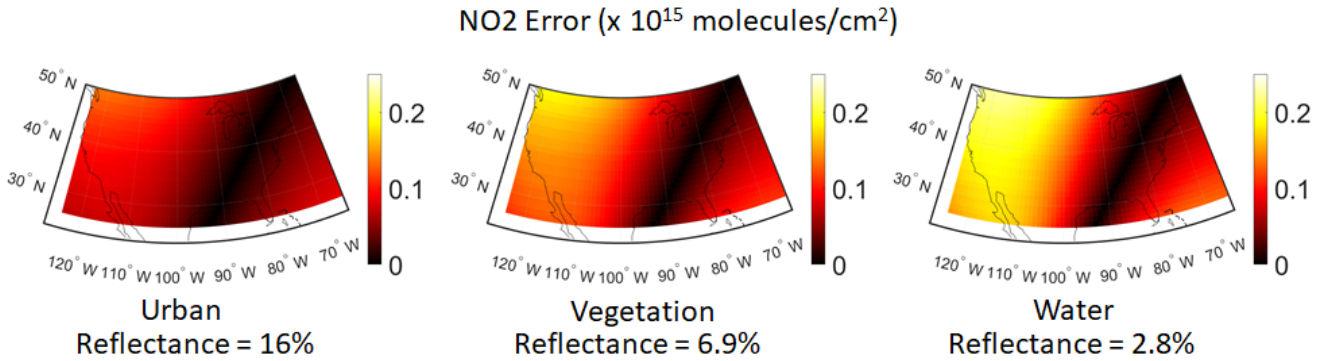


Figure 7. NO₂ errors assuming different scene types across CONUS for 5% PS in a vertical orientation and constant NO₂ profiles with 8.4×10^{15} molecules/cm²

The NO₂ errors derived decreased as the NO₂ amount decreased. This is shown in Fig. 8 for three different total vertical amounts: 5.9, 8.4, and 20×10^{15} molecules/cm². The retrieved amount is shown as a function of PS for two different orientations for selected US locations. The figure also shows the dependence on the time of day; the edge of the darker shading shows 230 the retrieved NO₂ amount with a solar zenith angle of 30° and the edge of the lighter shading shows the amount with an angle of 70° . The horizontal orientation results are similar to those for the vertical orientation. As evident in the previous results, the largest NO₂ errors occur in the western regions (Seattle, San Diego) for these orientations. The lower solar zenith angle corresponds to lower linear degree of linear polarization, accounting for the lower NO₂ errors.

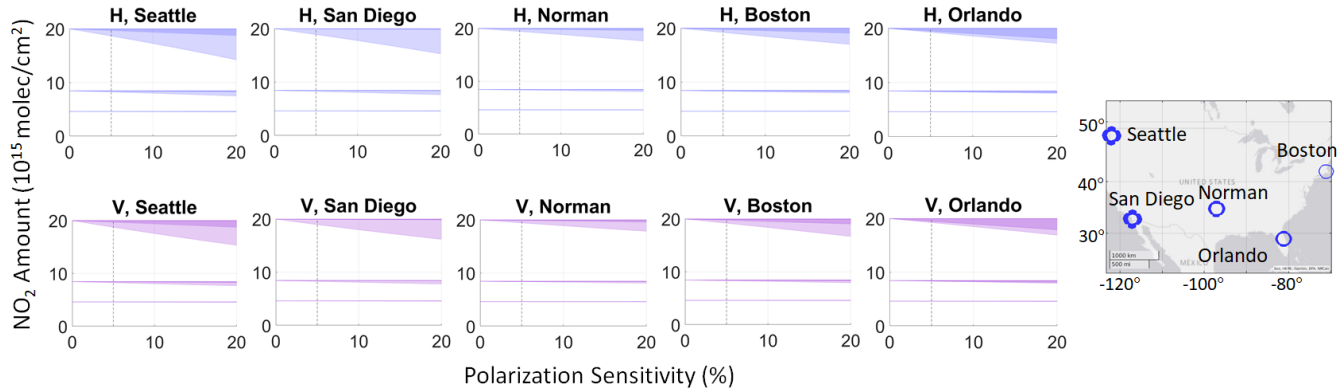


Figure 8. (Left) The retrieved amount is shown as a function of polarization sensitivity (PS) for two different orientations (H - horizontal, V - vertical) for selected US locations and NO₂ total vertical amounts: 5.0, 8.6, and 20×10^{15} molec/cm². The edge of the darker (lighter) shading shows the retrieved NO₂ amount with a solar zenith angle of 30° (70°). The vertical dotted line shows the current PS requirement for reference. (Right) The locations are shown on the map with thicker circles representing higher NO₂ errors

Fig. 9 shows the results using GEOS-5 profiles, which appear qualitatively consistent with the results using the artificial profiles used above. The NO₂ amounts for this day varied between 2.5 to 6.5×10^{15} molec/cm². The figure shows the polarization impacts with 5% PS in the vertical orientation. The impacts are more apparent as the solar zenith angle increases and resemble the previous results in Fig. 7, where the solar zenith angle is fixed at 70°. For instance, the NO₂ errors are larger at 20 UTC in the eastern regions where the solar angles are relatively large, and the NO₂ errors are larger in the western regions at UTC 16 where the solar zenith angles are larger. The higher cloud fraction decrease the retrieval errors, which can be seen in the western regions at 16 UTC; although the southwest and southeast have similar solar zenith angles, the southwest has lower retrieval errors due to the increased cloud fraction. The maximum NO₂ errors found were 0.03×10^{15} molec/cm² for this day —a negligible value when compared to the TEMPO precision requirement.

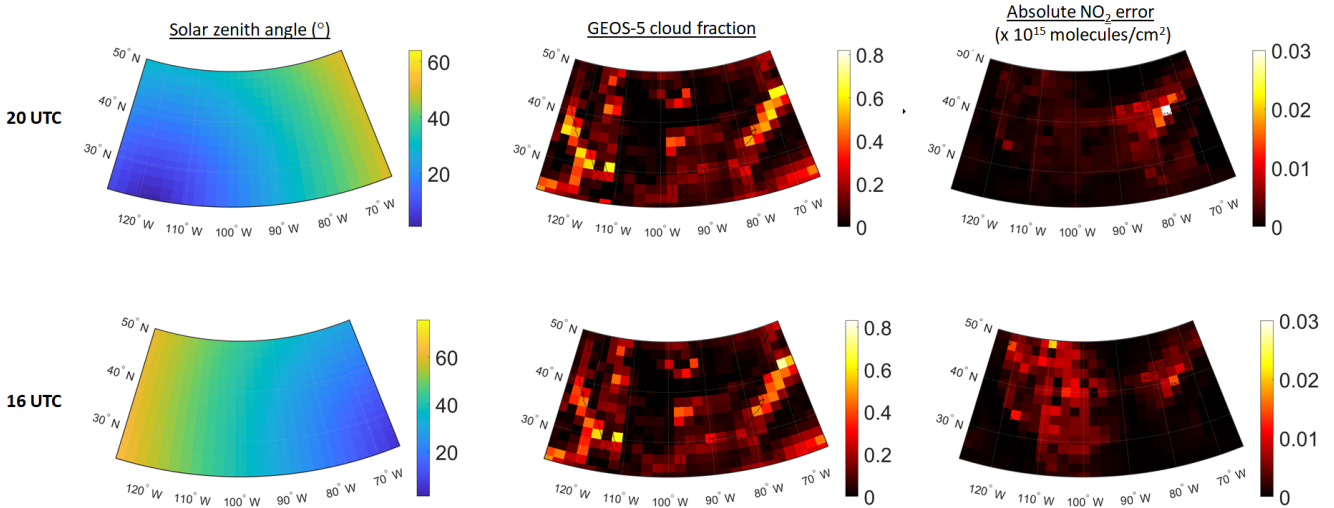


Figure 9. Solar zenith angles, GOES-5 cloud fraction, and resulting NO₂ errors at 20 UTC (top) and 16 UTC (bottom). GEOS-5 NO₂ profiles were used assuming 5% PS with vertical orientation, all water scenes, and clouds at a 2 km altitude.

4 Summary and conclusions

We demonstrated a simulation and modeling capability to assess polarization effects for ACX predicted performance studies.

245 Our results show that the DOAS spectral fitting step mitigates PS effects in the NO₂ retrieval process. The AMF calculation step, however, can cause retrieval errors from instrument PS when considering partially cloudy scenes. The PS magnitude and orientation (Mueller matrix elements) impacts can cause different NO₂ retrieval errors depending on location, time of day, cloud fraction, and NO₂ amount. For a PS of 5 % with vertical orientation, the maximum NO₂ retrievals errors were 0.25 $\times 10^{15}$ molecules/cm² for high pollution cases. In extreme cases, if NO₂ pollution significantly increases to levels on 250 the order of the world's most polluted regions, these errors can reach 1.4 $\times 10^{15}$ molecules/cm². A more typical maximum error found through analyzing the GEOS-5 profiles was 0.03 $\times 10^{15}$ molecules/cm². This study shows that in most cases, the 5% PS requirement introduces retrieval uncertainties significantly lower than the TEMPO precision requirement except in the most extreme cases. Note that these estimates assume a particular instrument Mueller matrix elements. We emphasized vertical orientation based on an assumed vertical grating orientation, where the instrument effectively sweeps wavelengths over 255 locations in the west-east direction. The Mueller matrix will be updated with the appropriate values as the instrument design matures to refine the estimates of NO₂ retrieval impacts. We note that our simplified retrieval approach may have neglected factors used in operational retrievals that could be affected by instrument PS and contribute to additional retrieval errors. This capability can be utilized to support the development of ACX to continue and build on the legacy of atmospheric composition measurements to forecast and monitor air quality.

260 *Author contributions.* Conceptualization, J.J., J.M., A.P., F.P.; methodology, J.J., A.P., M.C., B.E., L.L.; formal analysis, A.P., M.C.; resources, J.J., J.M. ; writing—original draft preparation, A.P.; writing—review and editing, A.P., J.J., M.C., F.P., L.L. ; software, B.E., L.L.; supervision, J.J., J.M.; project administration, J.J., J.M. All authors have read and agreed to the published version of the manuscript.

Competing interests. We declare that the authors have no conflicts of interest.

265 *Acknowledgements.* Xiong Lu and Kelly Chance assisted with ACX instrument model parameterization. Xiaoguang Xu and Jun Wang supplied and assisted with the UNL-VRTM code.

References

WHO global air quality guidelines particulate matter (PM2.5 and PM10), ozone, nitrogen dioxide, sulfur dioxide and carbon monoxide, WHO European Centre for Environment and Health, Bonn, Germany, 2021.

270 Bak, J., Liu, X., Kim, J.-H., Haffner, D. P., Chance, K., Yang, K., and Sun, K.: Characterization and correction of OMPS nadir mapper measurements for ozone profile retrievals, *Atmospheric Measurement Techniques*, 10, 4373–4388, <https://doi.org/10.5194/amt-10-4373-2017>, 2017.

Baldridge, A., Hook, S., Grove, C., and Rivera, G.: The ASTER spectral library version 2.0, *Remote Sensing of Environment*, 113, 711–715, <https://doi.org/10.1016/j.rse.2008.11.007>, 2009.

275 Berk, A., van den Bosch, J., Acharya, P., Adler-Golden, S., Anderson, G., and et al., L. B.: Algorithm Theoretical Basis Document (ATBD) for Next Generation MODTRAN, Spectral Sciences, Inc. Rpt. No. SSI-TR-688 (3247), Contract No. FA9453-12-C-0262, submitted to AFRL for publication, 2016.

Boersma, K. F., Eskes, H. J., Veefkind, J. P., Brinksma, E. J., van der A, R. J., Sneep, M., van den Oord, G. H. J., Levelt, P. F., Stammes, P., Gleason, J. F., and Bucsela, E. J.: Near-real time retrieval of tropospheric NO₂ from OMI, *Atmospheric Chemistry and Physics*, 7, 2103–2118, <https://doi.org/10.5194/acp-7-2103-2007>, 2007.

280 Bovensmann, H., Burrows, J. P., Buchwitz, M., Frerick, J., Noël, S., Rozanov, V. V., Chance, K. V., and Goede, A. P. H.: SCIAMACHY: Mission objectives and measurement modes, *Journal of the Atmospheric Sciences*, 56, 127 – 150, [https://doi.org/10.1175/1520-0469\(1999\)056<0127:SMOAMM>2.0.CO;2](https://doi.org/10.1175/1520-0469(1999)056<0127:SMOAMM>2.0.CO;2), 1999.

Bovensmann, H., Aben, I., Van Roozendael, M., Kühl, S., Gottwald, M., von Savigny, C., Buchwitz, M., Richter, A., Frankenberg, C., Stammes, P., de Graaf, M., Wittrock, F., Sinnhuber, M., Sinnhuber, B. M., Schönhardt, A., Beirle, S., Gloudemans, A., Schrijver, H., 285 Bracher, A., Rozanov, A. V., Weber, M., and Burrows, J. P.: SCIAMACHY's view of the changing Earth's environment, in: SCIAMACHY - Exploring the changing Earth's atmosphere, edited by Gottwald, M. and Bovensmann, H., pp. 175–216, Springer Netherlands, Dordrecht, https://doi.org/10.1007/978-90-481-9896-2_10, 2011.

Bucsela, E., Celarier, E., Wenig, M., Gleason, J., Veefkind, J., Boersma, K., and Brinksma, E.: Algorithm for NO/sub 2/ vertical column retrieval from the ozone monitoring instrument, *IEEE Transactions on Geoscience and Remote Sensing*, 44, 1245–1258, <https://doi.org/10.1109/tgrs.2005.863715>, 2006.

290 Burrows, J. P., Weber, M., Buchwitz, M., Rozanov, V., Ladstätter-Weißenmayer, A., Richter, A., DeBeek, R., Hoogen, R., Bramstedt, K., Eichmann, K.-U., Eisinger, M., and Perner, D.: The Global Ozone Monitoring Experiment (GOME): Mission concept and first scientific results, *Journal of the Atmospheric Sciences*, 56, 151 – 175, [https://doi.org/10.1175/1520-0469\(1999\)056<0151:TGOME>2.0.CO;2](https://doi.org/10.1175/1520-0469(1999)056<0151:TGOME>2.0.CO;2), 1999.

295 Cooper, M. J., Martin, R. V., Hammer, M. S., Levelt, P. F., Veefkind, P., Lamsal, L. N., Krotkov, N. A., Brook, J. R., and McLinden, C. A.: Global fine-scale changes in ambient NO₂ during COVID-19 lockdowns, *Nature*, 601, 380–387, <https://doi.org/10.1038/s41586-021-04229-0>, 2022.

Farrand, W.: Mapping the distribution of mine tailings in the Coeur d'Alene River Valley, Idaho, through the use of a constrained energy minimization technique, *Remote Sensing of Environment*, 59, 64–76, [https://doi.org/10.1016/s0034-4257\(96\)00080-6](https://doi.org/10.1016/s0034-4257(96)00080-6), 1997.

300 Goldin, D., Xiong, X., Shea, Y., and Lukashin, C.: CLARREO Pathfinder/VIIRS Intercalibration: Quantifying the Polarization Effects on Reflectance and the Intercalibration Uncertainty, *Remote Sensing*, 11, 1914, <https://doi.org/10.3390/rs11161914>, 2019.

Hollingsworth, A., Engelen, R. J., Textor, C., Benedetti, A., Boucher, O., Chevallier, F., Dethof, A., Elbern, H., Eskes, H., Flemming, J., Granier, C., Kaiser, J. W., Morcrette, J.-J., Rayner, P., Peuch, V.-H., Rouil, L., Schultz, M. G., and and, A. J. S.: TOWARD A MONITORING AND FORECASTING SYSTEM FOR ATMOSPHERIC COMPOSITION, *Bulletin of the American Meteorological Society*, 89, 1147–1164, <https://doi.org/10.1175/2008bams2355.1>, 2008.

305 Huangfu, P. and Atkinson, R.: Long-term exposure to NO₂ and O₃ and all-cause and respiratory mortality: A systematic review and meta-analysis, *Environment International*, 144, 105 998, <https://doi.org/10.1016/j.envint.2020.105998>, 2020.

Joiner, J.: Retrieval of cloud pressure and oceanic chlorophyll content using Raman scattering in GOME ultraviolet spectra, *Journal of Geophysical Research*, 109, <https://doi.org/10.1029/2003jd003698>, 2004.

310 Kokaly, R. F., Clark, R. N., Swayze, G. A., Livo, K. E., Hoefen, T. M., Pearson, N. C., Wise, R. A., Benzel, W. M., Lowers, H. A., Driscoll, R. L., and Klein, A. J.: USGS Spectral Library Version 7, <https://doi.org/10.3133/ds1035>, 2017.

Kolm, M. G., Maurer, R., Sallusti, M., Bagnasco, G., Gulde, S. T., Smith, D. J., and Courrèges-Lacoste, G. B.: Sentinel 4: a geostationary imaging UVN spectrometer for air quality monitoring: status of design, performance and development, in: *International Conference on Space Optics — ICSO 2014*, edited by Cugny, B., Sodnik, Z., and Karafolas, N., SPIE, <https://doi.org/10.1117/12.2304099>, 2017.

315 Kuhlmann, G., Lam, Y. F., Cheung, H. M., Hartl, A., Fung, J. C. H., Chan, P. W., and Wenig, M. O.: Development of a custom OMI NO₂ data product for evaluating biases in a regional chemistry transport model, *Atmospheric Chemistry and Physics*, 15, 5627–5644, <https://doi.org/10.5194/acp-15-5627-2015>, 2015.

Lamsal, L. N., Krotkov, N. A., Vasilkov, A., Marchenko, S., Qin, W., Yang, E.-S., Fasnacht, Z., Joiner, J., Choi, S., Haffner, D., Swartz, W. H., Fisher, B., and Bucsela, E.: Ozone Monitoring Instrument (OMI) Aura nitrogen dioxide standard product version 4.0 with improved surface 320 and cloud treatments, *Atmos. Meas. Tech.*, 14, 455–479, <https://doi.org/10.5194/amt-14-455-2021>, 2021.

Levelt, P., van den Oord, G., Dobber, M., Malkki, A., Visser, H., de Vries, J., Stammes, P., Lundell, J., and Saari, H.: The ozone monitoring instrument, *IEEE Transactions on Geoscience and Remote Sensing*, 44, 1093–1101, <https://doi.org/10.1109/TGRS.2006.872333>, 2006.

325 Levelt, P. F., Joiner, J., Tamminen, J., Veefkind, J. P., Bhartia, P. K., Stein Zweers, D. C., Duncan, B. N., Streets, D. G., Eskes, H., van der A, R., McLinden, C., Fioletov, V., Carn, S., de Laat, J., DeLand, M., Marchenko, S., McPeters, R., Ziemke, J., Fu, D., Liu, X., Pickering, K., Apituley, A., González Abad, G., Arola, A., Boersma, F., Chan Miller, C., Chance, K., de Graaf, M., Hakkarainen, J., Hassinen, S., Ialongo, I., Kleipool, Q., Krotkov, N., Li, C., Lamsal, L., Newman, P., Nowlan, C., Suleiman, R., Tilstra, L. G., Torres, O., Wang, H., and Wargan, K.: The Ozone Monitoring Instrument: Overview of 14 years in space, *Atmos. Chem. Phys.*, 18, 5699–5745, <https://doi.org/10.5194/acp-18-5699-2018>, 2018.

Marchenko, S., Krotkov, N. A., Lamsal, L. N., Celarier, E. A., Swartz, W. H., and Bucsela, E. J.: Revising the slant column density retrieval 330 of nitrogen dioxide observed by the Ozone Monitoring Instrument, *Journal of Geophysical Research: Atmospheres*, 120, 5670–5692, <https://doi.org/10.1002/2014JD022913>, 2015.

Martin, R. V.: An improved retrieval of tropospheric nitrogen dioxide from GOME, *Journal of Geophysical Research*, 107, <https://doi.org/10.1029/2001jd001027>, 2002.

Meerdink, S. K., Hook, S. J., Roberts, D. A., and Abbott, E. A.: The ECOSTRESS spectral library version 1.0, *Remote Sensing of Environment*, 230, 111 196, <https://doi.org/10.1016/j.rse.2019.05.015>, 2019.

335 Meister, G. and Franz, B. A.: Adjustments to the MODIS Terra radiometric calibration and polarization sensitivity in the 2010 reprocessing, in: *Earth Observing Systems XVI*, edited by Butler, J. J., Xiong, X., and Gu, X., SPIE, <https://doi.org/10.1117/12.891787>, 2011.

Molod, A., Takacs, L., Suarez, M., Bacmeister, J., Song, I.-S., and Eichmann, A.: The GEOS-5 atmospheric general circulation model: Mean climate and development from MERRA to Fortuna, *Tech. rep.*, 2012.

340 Munro, R., Lang, R., Klaes, D., Poli, G., Retscher, C., Lindstrot, R., Huckle, R., Lacan, A., Grzegorski, M., Holdak, A., Kokhanovsky, A.,
Livschitz, J., and Eisinger, M.: The GOME-2 instrument on the Metop series of satellites: instrument design, calibration, and level 1 data
processing – an overview, *Atmospheric Measurement Techniques*, 9, 1279–1301, <https://doi.org/10.5194/amt-9-1279-2016>, 2016.

Pearlman, A. J., Cao, C., and Wu, X.: The GOES-R Advanced Baseline Imager: polarization sensitivity and potential impacts, in: *Polarization
Science and Remote Sensing VII*, edited by Shaw, J. A. and LeMaster, D. A., SPIE, <https://doi.org/10.1117/12.2188508>, 2015.

345 Richter, A. and Burrows, J.: Tropospheric NO₂ from GOME measurements, *Advances in Space Research*, 29, 1673–1683,
[https://doi.org/10.1016/S0273-1177\(02\)00100-X](https://doi.org/10.1016/S0273-1177(02)00100-X), 2002.

Shettle, E., Fenn, R., and Laboratory, U. A. F. G.: Models for the Aerosols of the Lower Atmosphere and the Effects of Humidity Variations
on Their Optical Properties, AFGL-TR, Air Force Geophysics Laboratory, Air Force Systems Command, United States Air Force, <https://books.google.com/books?id=UoXkXweSrQEC>, 1979.

350 Shindell, D. T., Faluvegi, G., Koch, D. M., Schmidt, G. A., Unger, N., and Bauer, S. E.: Improved attribution of climate forcing to emissions,
Science, 326, 716–718, <https://doi.org/10.1126/science.1174760>, 2009.

Stammes, P., Sneed, M., de Haan, J. F., Veefkind, J. P., Wang, P., and Levelt, P. F.: Effective cloud fractions from the Ozone Monitoring
Instrument: Theoretical framework and validation, *Journal of Geophysical Research*, 113, <https://doi.org/10.1029/2007jd008820>, 2008.

355 Valks, P., Pinardi, G., Richter, A., Lambert, J.-C., Hao, N., Loyola, D., Van Roozendael, M., and Emmadi, S.: Operational total and tropo-
spheric NO₂ column retrieval for GOME-2, *Atmospheric Measurement Techniques*, 4, 1491–1514, <https://doi.org/10.5194/amt-4-1491-2011>, 2011.

van Geffen, J., Boersma, K. F., Eskes, H., Sneed, M., ter Linden, M., Zara, M., and Veefkind, J. P.: S5P TROPOMI NO₂ slant col-
umn retrieval: method, stability, uncertainties and comparisons with OMI, *Atmospheric Measurement Techniques*, 13, 1315–1335,
<https://doi.org/10.5194/amt-13-1315-2020>, 2020.

360 Vasilkov, A., Joiner, J., Spurr, R., Bhartia, P. K., Levelt, P., and Stephens, G.: Evaluation of the OMI cloud pressures derived from rotational
Raman scattering by comparisons with other satellite data and radiative transfer simulations, *Journal of Geophysical Research*, 113,
<https://doi.org/10.1029/2007jd008689>, 2008.

Veefkind, J., Aben, I., McMullan, K., Förster, H., de Vries, J., Otter, G., Claas, J., Eskes, H., de Haan, J., Kleipool, Q., van Weele, M.,
365 Hasekamp, O., Hoogeveen, R., Landgraf, J., Snel, R., Tol, P., Ingmann, P., Voors, R., Kruizinga, B., Vink, R., Visser, H., and Levelt, P.:
TROPOMI on the ESA Sentinel-5 Precursor: A GMES mission for global observations of the atmospheric composition for climate, air
quality and ozone layer applications, *Remote Sensing of Environment*, 120, 70–83, <https://doi.org/10.1016/j.rse.2011.09.027>, 2012.

370 Wu, A., Geng, X., Wald, A., Angal, A., and Xiong, X.: Assessment of Terra MODIS On-Orbit Polarization Sensitivity Using Pseudoinvariant
Desert Sites, *IEEE Transactions on Geoscience and Remote Sensing*, 55, 4168–4176, <https://doi.org/10.1109/tgrs.2017.2689719>, 2017.

Xu, X. and Wang, J.: UNL-VRTM, A Testbed for Aerosol Remote Sensing: Model Developments and Applications, in: *Springer Series in
Light Scattering*, pp. 1–69, Springer International Publishing, https://doi.org/10.1007/978-3-030-20587-4_1, 2019.

Yan, X., Zang, Z., Zhao, C., and Husi, L.: Understanding global changes in fine-mode aerosols during 2008–2017 using statistical methods
and deep learning approach, *Environment International*, 149, 106392, <https://doi.org/10.1016/j.envint.2021.106392>, 2021.

Zoogman, P., Liu, X., Suleiman, R., Pennington, W., Flittner, D., Al-Saadi, J., Hilton, B., Nicks, D., Newchurch, M., Carr, J., Janz, S.,
Andraschko, M., Arola, A., Baker, B., Canova, B., Miller, C. C., Cohen, R., Davis, J., Dussault, M., Edwards, D., Fishman, J., Ghu-
375 lam, A., Abad, G. G., Grutter, M., Herman, J., Houck, J., Jacob, D., Joiner, J., Kerridge, B., Kim, J., Krotkov, N., Lamsal, L., Li,
C., Lindfors, A., Martin, R., McElroy, C., McLinden, C., Natraj, V., Neil, D., Nowlan, C., OSullivan, E., Palmer, P., Pierce, R., Pip-
pin, M., Saiz-Lopez, A., Spurr, R., Szykman, J., Torres, O., Veefkind, J., Veihelmann, B., Wang, H., Wang, J., and Chance, K.: Tro-

pospheric emissions: Monitoring of pollution (TEMPO), Journal of Quantitative Spectroscopy and Radiative Transfer, 186, 17–39, <https://doi.org/10.1016/j.jqsrt.2016.05.008>, 2017.